

The accreted stellar haloes of Milky Way-mass galaxies as a probe of the nature of the dark matter

Victor J. Forouhar Moreno^{1,2*}, Azadeh Fattahi², Alis J. Deason², Fergus Henstridge² and Alejandro Benítez-Llambay³.

¹*Leiden Observatory, Leiden University, Leiden 2333 CC, Netherlands*

²*Institute for Computational Cosmology, Department of Physics, Durham University, Durham DH1 3LE, UK*

³*University of Milano-Bicocca, Piazza della Scienza, 3, 20126 Milano MI, Italy*

Accepted XXX. Received YYY; in original form ZZZ

ABSTRACT

Galactic stellar haloes are largely composed of the remnants of galaxies accreted during the assembly of their host galaxies, and hence their properties reflect the mass spectrum and post-accretion evolution of their satellites. As the nature of dark matter (DM) can affect both, we explore how the properties of the accreted stellar component vary across cold (CDM), warm (WDM) and self-interacting (SIDM) models. We do this by studying accreted stellar populations around eight MW-mass haloes using cosmological hydrodynamical simulations based on the EAGLE galaxy formation model, in which we find that the accreted stellar mass remains similar across models. Contrary to WDM, which only presents minor differences relative to CDM, the distribution of accreted stars in SIDM changes significantly within $0.05R_{200}$ (10 kpc). The central density reduces to $\langle \rho_{\text{exsitu}}^{\text{SIDM}} / \rho_{\text{exsitu}}^{\text{CDM}} \rangle = 0.3$ and has a shallower radial dependence, with logarithmic density slopes of $\langle \alpha_{\text{SIDM}} \rangle = -1.4$ vs $\langle \alpha_{\text{CDM}} \rangle = -1.7$. Additionally, stars are on more tangential orbits than their CDM counterparts, with a change in the velocity anisotropy of $\langle \Delta\beta \rangle = -0.2$. Finally, SIDM stellar haloes have the largest number and prominence of overdensities in radius vs radial velocity space. This is due to a combination of shorter stellar halo progenitor merging timescales and shallower host potentials, with the former resulting in less time for dynamical friction and radialisation to operate. In summary, we show that the phase-space structure of Galactic stellar haloes encode key information that can be used to distinguish and rule out different DM models.

Key words: dark matter, galaxies: haloes

1 INTRODUCTION

Structure formation within the Λ CDM model proceeds in a hierarchical fashion (Davis et al. 1985), whereby small structures form first and then grow larger through mass accretion and mergers. This process results in the formation of virialised structures, known as dark matter haloes, that follow quasi-universal density profiles (Navarro et al. 1997) over twenty orders of magnitude in halo mass (Wang et al. 2020). Haloes can grow in mass discretely by the accretion of neighbouring dark matter haloes, which are not necessarily disrupted. Their subsequent evolution after being accreted depends on their mass relative to their host, their orbital and structural parameters, and the nature of the dark matter itself (e.g. halos could evaporate as they merge if the dark matter has a non-zero interaction cross-section; Kummer et al. 2018). Those sufficiently massive to experience dynamical friction (Chandrasekhar 1943) lose orbital angular momentum and energy, eventually disrupting in the core of the host. The remaining objects are primarily affected by tidal stripping and shock heating. The loss of mass that occurs during merging and stripping can lead to the formation of streams and shells of material, leaving an imprint in phase space that can remain long after they first formed.

In the context of Milky Way (MW)-mass haloes, the hierarchical growth of structure means that stars stripped from accreted galaxies form stellar streams, shells and a dynamically hot halo of stars (e.g. Helmi & White 1999; Diemand et al. 2005; Bullock & Johnston 2005; Abadi et al. 2006). Stellar haloes have been detected in external galaxies (e.g. Radburn-Smith et al. 2011; Gilbert et al. 2014; Merritt et al. 2016) and around the Milky Way. The stellar halo of our Galaxy is estimated to contain one per cent of the stellar mass (Deason et al. 2019), and it is composed both by stars accreted from merged and stripped satellites (*ex-situ*; e.g. Bell et al. 2008), as well as stars that formed within the Milky Way and whose orbits were subsequently heated (*in-situ*; e.g. Purcell et al. 2010; Cooper et al. 2015).

The advent of precision astrometric and spectroscopic surveys such as GAIA (Gaia Collaboration et al. 2016a,b, 2018, 2023), APOGEE (Majewski et al. 2017) and H3 (Conroy et al. 2019) have helped unravel the assembly history of our Galaxy using its stellar halo. Evidence for an ancient major merger (Deason et al. 2013) has been strengthened thanks to these data (Helmi et al. 2018; Belokurov et al. 2018), with less massive events also being detected through their imprints in chemistry and action-space (e.g. Koppelman et al. 2019; Naidu et al. 2020).

The prospect of leveraging the information contained within the stellar halo for galactic archaeology (Eggen et al. 1962; Searle & Zinn 1978) has motivated studies seeking to establish a connection

* E-mail: forouhar@strw.leidenuniv.nl

between its properties, e.g. mass, metallicity and density profiles, to how it assembled. Additionally, the large spatial extent of stellar haloes also makes them powerful tracers of the underlying gravitational potential (e.g. Johnston et al. 1999), thus helping constrain the mass (e.g. Deason et al. 2021; Genina et al. 2023), shape (e.g. Boy et al. 2016) and distortions (e.g. Erkal et al. 2021) of the dark matter halo surrounding the Milky Way.

An underlying assumption in most studies concerning the stellar halo of the Milky Way is that the dark matter is cold and collisionless. Cold dark matter (CDM), initially motivated by promising extensions to the Standard Model (Ellis et al. 1984), became the *de-facto* dark matter model as a result of the agreement between the predicted and observed properties of large scale cosmic structure (e.g. Cole et al. 2005; Springel et al. 2006; Rodríguez-Torres et al. 2016). However, none of the proposed particle candidates have been detected yet (e.g. Aprile et al. 2018; Canepa 2019), making viable alternatives to CDM an attractive prospect worth exploring.

Models that differ from CDM do so primarily in their small scale predictions. For example, the cut-off in the matter power spectrum present in warm dark matter models (WDM) suppresses the formation of structure below the corresponding mass scale (Bode et al. 2001). The changing power spectrum also has structural implications, such as lower halo concentrations resulting from a delay in the formation time of haloes (e.g. Bose et al. 2017). For currently viable models of WDM, these changes are relegated to the dwarf galaxy regime.

The effects of a self-interacting model of dark matter (SIDM; Spergel & Steinhardt 2000) primarily affect the matter distribution where DM densities are large enough to sustain a high rate of scattering. These regions correspond to the centres of dark matter haloes, which develop flatter density profiles with a rounder configuration (e.g. Davé et al. 2001) than their CDM counterparts, so long as the cross-section is not large enough to trigger gravothermal collapse. More elaborate models also result, as is the case in WDM, in a power spectrum cut-off on small scales (Vogelsberger et al. 2016; Cyr-Racine et al. 2016).

The differences arising in competing models of DM propagate to the halos and galaxies that have been accreted by more massive systems. The suppression in the formation of low-mass haloes affects how many satellites a given Milky Way-mass host can accrete throughout its lifetime. Differences in the inner density profile are expected to affect how efficient mass-stripping due to gravitational tides is (e.g. Peñarrubia et al. 2010). As such, the abundance and distribution of the present day Milky Way satellites may provide a way to constrain the properties of the dark matter (e.g. Kennedy et al. 2014; Lovell et al. 2014; Newton et al. 2021; Nadler et al. 2021), modulo the uncertainties introduced by the effect of baryons and its coupling to the surrounding DM (Forouhar Moreno et al. 2022), like supernovae-feedback on dwarf scales (e.g. Navarro et al. 1996; Pontzen & Governato 2012; Di Cintio et al. 2014; Read et al. 2018).

Since the formation of the stellar halo is intimately related to the stripping and disruption of satellite galaxies, changing how many are accreted and how efficiently they are stripped from stars may result in noticeable differences in the properties of stellar haloes. For example, the suppression of the least massive satellites could affect the number of accreted stars in the outer stellar halo, as these are the progenitors that dominate its outskirts (e.g. Fattahi et al. 2020). Additionally, changing the structural parameters of haloes hosting dwarf galaxies can alter the spatial distribution and kinematics of the resulting remnant (Amorisco 2017; Vasiliev et al. 2022).

Given the potential importance of the assumed nature of DM on the properties of stellar halos, it is surprising that few studies have

explored the connection between the two in detail. Beyond stream ‘gapology’ (e.g. Ibata et al. 2002) and stellar wakes (e.g. Buschmann et al. 2018), the most recent example focused on the stellar haloes around dwarf galaxies using idealised N-body simulations (Deason et al. 2022). However, this mass scale is subject to substantial theoretical (e.g. Brook et al. 2014; Read et al. 2017; Jethwa et al. 2018; Graus et al. 2019; Benitez-Llambay & Frenk 2020) and observational uncertainties (e.g. Kazantzidis et al. 2011; Sestito et al. 2023; Waller et al. 2023).

Addressing the question of whether the nature of dark matter systematically affects the stellar halo of Milky Way-mass galaxies is particularly important due to ongoing and upcoming surveys, such as WEAVE (Jin et al. 2023), DESI MWS (Cooper et al. 2023), Vera Rubin LSST (Ivezić et al. 2019) and ARRAKIHS (Guzmán et al. 2022). These surveys will provide a wealth of data concerning the stellar halo surrounding external galaxies and the outskirts of our own. The larger sample size will provide a way of studying the statistical properties of stellar haloes around Milky Way-mass galaxies and, hence, be less dominated by the atypical assembly history of our own (Evans et al. 2020). This is a crucial step towards using them as dark matter probes since the stochasticity in their assembly histories leads to changes comparable to those caused by alternative dark matter models (Power & Robotham 2016).

To explore how the stellar halo properties depend on the nature of the dark matter, we study eight different Milky Way-mass haloes formed within high-resolution hydrodynamical simulations based on the EAGLE model of galaxy formation. The only changes across the three cosmological simulations we consider in this work concern the assumed nature of dark matter. This allows us to study the same set of stellar haloes in cold, warm and self-interacting dark matter models, decoupling the effect of different assembly histories by matching haloes to their fiducial CDM counterparts.

We begin by introducing the simulations and galaxy formation model we used in this study, followed by the operational definitions we use to identify stellar haloes. In Section 4.1, we explore the present-day masses of these stellar haloes, how they compare with our own Galaxy, and whether they are sensitive to the nature of dark matter. We then proceed to investigate their spatial (§4.2) and dynamical (§4.3) properties. Lastly, in Section 4.4, we discuss how differences in the progenitors of the stellar halos have resulted in the observed changes in their present-day properties.

2 SIMULATIONS

In this section, we describe the simulation code, galaxy formation physics and alternative dark matter models used in our simulations.

2.1 The galaxy formation model

We have run our smoothed particle hydrodynamics simulations using the version of P-Gadget3 (Springel 2005) that includes the galaxy formation physics of the EAGLE project (Schaye et al. 2015; Crain et al. 2015). The EAGLE model, which reproduces a number of observed population statistics (e.g. Schaller et al. 2015; Ludlow et al. 2017), incorporates subgrid prescriptions for the physics relevant to galaxy formation and evolution: radiative cooling and photoheating (Wiersma et al. 2009), star formation and evolution (Schaye 2004; Schaye & Dalla Vecchia 2008), stellar feedback (Dalla Vecchia & Schaye 2012), black hole seeding (Springel et al. 2005; Booth & Schaye 2009) & its subsequent growth and stochastic, thermal AGN feedback.

The values of the parameters used in modelling these processes were set by requiring a good match to the observed $z = 0.1$ galaxy stellar mass function, the distribution of galaxy sizes and the amplitude of the central black hole mass *vs* stellar mass relation. For this work, we use the calibration made for the higher mass resolution version of EAGLE (RECAL in the nomenclature of Schaye et al. 2015).

We simulate the evolution of structure in a periodic box of 12Mpc side-length from $z = 127$ to $z = 0$, assuming the cosmological parameter values of Planck Collaboration et al. (2014). We populate it with 2×512^3 particles, half of which are dark matter and the rest gas particles. This corresponds to a particle mass resolution of $m_{\text{DM}} = 4 \times 10^5 M_{\odot}$ and $m_{\text{gas}} = 8 \times 10^4 M_{\odot}$, respectively. The initial DM particle distribution was generated using MUSIC (Hahn & Abel 2011).

2.2 Warm dark matter

We obtain the power spectrum of WDM, $P_{\text{WDM}}(k) = T^2(k)P_{\text{CDM}}(k)$, using the transfer function of Bode et al. (2001):

$$T^2(k) = [1 + (\alpha k)^{2\nu}]^{-5/\nu}. \quad (1)$$

Here, ν is a fitting constant equal to 1.2 and the parameter α depends on the assumed mass of the WDM particle:

$$\alpha = 0.049 \left[\frac{m_{\text{th}}}{\text{keV}} \right]^{-1.11} \left[\frac{\Omega_{\text{WDM}}}{0.25} \right]^{0.11} \left[\frac{h}{0.7} \right]^{1.22} h^{-1} \text{Mpc}. \quad (2)$$

For this work we assume $m_{\text{th}} = 2.5 \text{ keV}$. This is lighter than the equivalent thermal relic mass of a 7 keV sterile neutrino model attributed through its decay to the unidentified 3.5 keV X-ray line (Boyarsky et al. 2014). Nonetheless, we chose this value to enhance the differences with respect to CDM to allow for an easier comparison. As a reference point, the Jean's mass of a perturbation with a wavelength equal to the one where the WDM power spectrum is half of the CDM one is $m_{1/2} = 1.4 \times 10^9 M_{\odot}$. This corresponds to the mass scale where the differences with respect to CDM are expected to be noticeable.

2.3 Self-interacting dark matter

Self-interactions are modelled using the Monte-Carlo implementation described in Robertson et al. (2017). Dark matter particles can scatter with each other when they are closer than the gravitational softening length of the simulations, ϵ . The probability of any two neighbouring particles scattering, within a timestep of size Δt , is a function of their relative velocity and the assumed cross-section, σ_{SIDM} :

$$P_{ij} = \frac{\sigma_{\text{SIDM}} |\vec{v}_i - \vec{v}_j|}{4\pi\epsilon^3} \quad (3)$$

In this study, we use a constant isotropic cross-section of $\sigma_{\text{SIDM}} = 10 \text{ cm}^2 \text{ g}^{-1}$.

3 METHODS

Here we discuss how we construct the catalogue of dark matter haloes and galaxies in our simulations. We also explain how we link them across time to build their merger trees, and how this information is used to identify the accreted stellar halo and its progenitor galaxies.

We also discuss how we remove the spurious structures that form in WDM (e.g. Wang & White 2007), and how we select our sample of host galaxies.

3.1 Structure finding and merger trees

To identify dark matter haloes, we assign particles into distinct groups according to the friends-of-friends (FoF) percolation algorithm (Davis et al. 1985). They are first found by linking every dark matter particle within 0.2 times their mean interparticle separation. The remaining particle types (gas, star and black holes) are then attached to the group of their nearest DM particle. Using the SUBFIND algorithm (Springel et al. 2001), the FoF groups are subdivided into candidate subhaloes by locating peaks in the smoothed density field and subjecting the enclosed particles to an iterative unbinding algorithm. Those which are self-bound and contain 20 or more particles comprise our catalogue of structures. The most massive subgroup in a given FoF group is chosen as its central galaxy, with the remaining ones labelled as satellites.

We follow the time evolution of all galaxies using their merger trees, which are built by cross-matching a subset of the most gravitationally-bound particles between consecutive time outputs (Jiang et al. 2014). The algorithm links galaxies that temporarily disappear from the catalogues up to five consecutive time outputs, prone to occur when near the centre of a more massive object. The main progenitor branch is then found by identifying the progenitor branch with the largest integrated mass (De Lucia & Blaizot 2007). This choice reduces the influence that central halo switching, prone to occur during major mergers, has on the identification of the main progenitor.

3.2 Spurious group removal

Particle-based simulations with a resolved power spectrum cut-off result in the spurious fragmentation of filaments due to the discrete representation of the underlying density field (Wang & White 2007). This artificially boosts the number of identified structures below the mass scale where structure formation is strongly suppressed. We therefore clean the WDM catalogues from these structures using the criteria of Lovell et al. (2014).

Firstly, we remove all subhaloes whose peak bound mass is lower than the scale where spurious structures are expected to dominate:

$$M_{\text{lim}} = 5.05 \bar{\rho} d k_{\text{peak}}^{-2}, \quad (4)$$

where d is the mean interparticle separation, k_{peak} the wavelength at which the dimensionless power spectrum peaks, and $\bar{\rho}$ is the mean density of the universe. For our setup, this corresponds to $M_{\text{lim}} = 1.4 \times 10^8 M_{\odot}$. Lastly, we compute the sphericity ($s \equiv c/a$, where c and a are the smallest and largest eigenvalues of the inertia tensor) of the Lagrangian region associated to the proto-haloes of the remaining subhaloes, using the particles bound to them when they first reached their half peak mass. Those with significantly flattened distributions ($s \leq 0.16$), and hence likely spurious, are removed.

3.3 Sample of host galaxies

As we are interested in studying the stellar haloes present in systems with masses similar to that of our own Milky Way, we restrict our

analysis to haloes of mass M_{200}^1 at $z = 0$ in the range $0.5 - 2.5 \times 10^{12} M_{\odot}$. This is within a factor of two from recent observational estimates of the Milky Way's halo mass (e.g. [Callingham et al. 2019](#); [Cautun et al. 2020](#)). A total of eight haloes satisfy this criterion in the simulated volume we use in this study.

3.4 Defining the stellar halo and its progenitors

There are several operational definitions used to identify stellar haloes within simulations. Some rely on cuts based on the spatial (e.g. [Monachesi et al. 2019](#)) and circularity distribution of stars (e.g. [Font et al. 2011](#)), and others do so based on whether the stars have been accreted from other galaxies (e.g. [Fattahi et al. 2020](#)). Choosing a particular definition reflects the questions one wants to address, which in our case concerns whether the assumed nature of dark matter affects the properties of the accreted stellar halo. As such, we define the stellar halo as being composed solely by accreted² stars.

In practice, reliably identifying which stars have formed in-situ and which have been accreted is not trivial. For instance, identifying which star particles are in-situ requires identifying the main progenitor of a given MW-mass galaxy chosen at $z = 0$. In this work we choose it to be the merger tree branch with the largest integrated mass. However, the concept of a dominant 'main progenitor' becomes less well-defined at high redshifts, and major mergers can result in the misidentification of which galaxy is the most massive. Additionally, configuration space-based structure finders can temporarily miss and artificially truncate galaxies when undergoing close pericentric passages. These factors often blur the boundary between in-situ and ex-situ material.

Our selection of stars to analyse is done at redshift $z = 0$, by identifying all stellar particles within the FoF groups hosting our sample of MW-mass haloes. To avoid including in our analysis the stellar component of self-bound satellites, we further require that particles are classified as bound to either the MW central galaxy (i.e. the most massive galaxy within its FoF group) or unbound. This results in a population that includes stars formed within the MW main progenitor and stars originating from the debris of dwarf satellites accreted in the past.

Since we are only interested in the accreted stellar component, we need to further clean the sample. We have explored two alternative ways to do so, one based on either the radial distance of stars to the Milky Way main progenitor (e.g. [Sanderson et al. 2018](#)) and the other on whether stars were bound to it (e.g. [Fattahi et al. 2020](#)), both measured when the star particle formed. Although the formation time of each simulated stellar particle is precisely known, only discrete outputs in time contain information about their spatial position or structure membership. This means that, in practice, we use the snapshot immediately before the star particle birth time and hence the position, velocity and bound membership from its parent gas particle.

By comparing the above methods, we found that the spatial criterion identified some stellar shells as in-situ. This is due to several progenitor galaxies forming stars during close pericentric passages, a process likely triggered by the compression of gas by its interaction with the host (e.g. [Genina et al. 2019](#)). We therefore use the bound membership of the gas particle to identify the accreted stellar

component, which correctly identified all the associated shells and streams as ex-situ.

4 RESULTS

4.1 Stellar halo masses

We begin by analysing how the accreted stellar mass varies across the galaxies in our sample, and examine if there is any dependence on the assumed model of dark matter. The ex-situ stellar masses for the galaxies formed in the CDM simulation are shown along the horizontal axis of Fig. 1, with the median and 16th - 84th percentiles of our sample being $M_{\text{exsitu}}^{\text{CDM}} = 2.1_{-0.7}^{+2.3} \times 10^9 M_{\odot}$. Although roughly consistent with observational estimates for the mass of the MW stellar halo, we note that our quoted value does not include the in-situ stellar halo. Hence, the masses we measure here represent a lower limit of total mass of our simulated stellar haloes.

We further note that half of our sample has an accreted stellar halo more massive than the total mass of the Milky Way stellar halo. As our simulated Milky Way analogues are only selected based on their present-day virial mass, it is likely that the galaxies in our sample formed later than counterparts whose assembly histories more closely match that of our Galaxy. As the mass of stellar haloes correlate with their time of formation (e.g. [Deason et al. 2019](#)), one might thus expect more massive stellar haloes in our sample. We further note that ex-situ mass fraction in our sample, defined here as the ratio of the ex-situ mass to the total stellar mass within a 30 kpc spherical aperture, is $\sim 21\%$ and hence significantly larger than the inferred $\sim 1\%$ for our Galaxy. Aside from the tendency for the accreted mass to be somewhat higher, this is also driven by the fact the EAGLE model of galaxy formation underpredicts the stellar masses of central galaxies that are hosted in Milky Way mass haloes.

Shifting our focus to the impact of the assumed nature of dark matter on the properties of the accreted stellar haloes, Fig 1 indicates that there are up to $\sim 20\%$ -level differences at a fixed stellar halo between the different DM models. Despite a tendency toward lower accreted masses, with a median ratio and scatter of $M_{\text{exsitu}}^{\text{WDM}}/M_{\text{exsitu}}^{\text{CDM}} = 0.9_{-0.2}^{+0.2}$ and $M_{\text{exsitu}}^{\text{SIDM}}/M_{\text{exsitu}}^{\text{CDM}} = 0.9_{-0.1}^{+0.1}$, the population is consistent with those found in CDM. The relatively small differences across the various DM models explored here indicates that the nature of DM plays a minor role in setting the *overall* ex-situ mass of the stellar halo. This is because the largest progenitors, which contribute most of the accreted mass, have similar stellar masses across the models, as shown in the appendix (Fig. A1). Nonetheless, it is worth remembering that we have not considered the in-situ component of the stellar halo. As such, our mass estimate corresponds to a lower bound of the total stellar halo mass, and does not imply that the total (ex-situ plus in-situ) remains similar across DM models.

We conclude that the total accreted mass of stellar haloes is largely insensitive to changes caused by the nature of the dark matter. The reason behind this similarity is the fact that neither warm nor self-interacting dark matter change the mass or abundance of the largest stellar halo progenitors. Since these dominate the mass budget of the stellar halo, their ex-situ masses do not change substantially across models. However, this does not preclude the presence of differences on a spatial or dynamical level, which we explore next.

4.2 Stellar density profiles

As shown in earlier work ([Forouhar Moreno et al. 2022](#)), the self-interactions between DM particles in our SIDM simulation lead to

¹ M_{200} is defined as the mass contained within a sphere of mean density 200 times the critical density of the universe.

² We use accreted and ex-situ interchangeably throughout this paper.

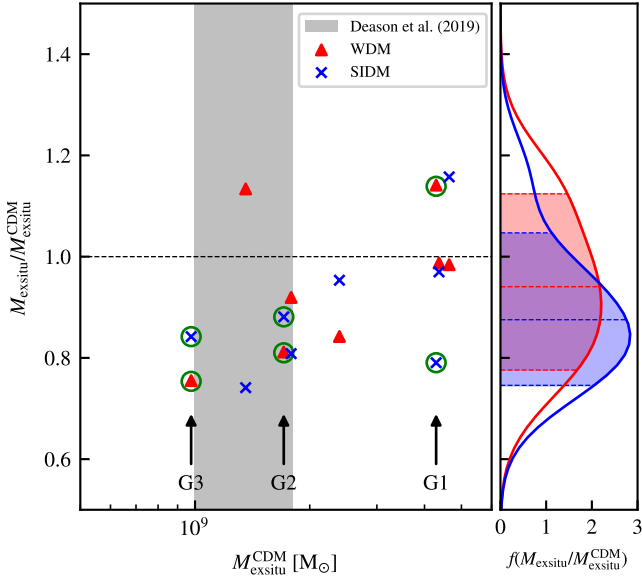


Figure 1. Ex-situ stellar mass for the eight MW-mass haloes in our sample. The location along the horizontal axis indicates their value in the CDM simulation, with the mass formed in the alternative DM counterparts expressed relative to their CDM values in the vertical axis. These are indicated by the red triangles and blue crosses for WDM and SIDM, respectively. The right panel shows the distribution function of the aforementioned quantities, after applying a kernel density estimate. The shaded regions enclose the 16th and 84th percentiles of each distribution, with the median value indicated by the corresponding dashed line. The grey bands correspond to the inferred stellar halo mass of the Milky Way (Deason et al. 2019). The three example galaxies discussed in §4.3 (G1, G2 and G3) are highlighted using green circles and vertical arrows.

the formation of flat inner density profiles in the haloes that host dwarf and MW-mass galaxies ($5 \times 10^9 \leq M_{200} \leq 2.5 \times 10^{12} M_{\odot}$). The change on dwarf-scales accelerates the deposition of stars in the stellar halo through more efficient stripping, as the presence of a flat density core makes DM haloes less resilient to gravitational tides, relative to steeper inner density profiles (e.g. Peñarrubia et al. 2010; Errani et al. 2022). On the other hand, the change on MW-scales modifies the underlying potential in which stars orbit. Thus, one might expect the spatial distribution of accreted stars to reflect these changes.

We explore this in the top panel of Fig. 2, which shows the median density profiles obtained from our sample of MW-mass haloes. We measure the profiles for each individual galaxy using 30 spherical shells whose edges are logarithmically spaced between $0.005R_{200}$ and R_{200} . We define the origin as the centre of mass of all dark matter particles within 5 kpc from the centre of potential of the main galaxy, as identified by SUBFIND. The spatial offset between this centre and the halo centre of potential (or the centre of mass of the stars) is comparable to the gravitational softening of the simulation.

Focusing first on the WDM model, the density profile of accreted stars displays only minor differences relative to the CDM counterparts. The profiles are similar across the radial extent we consider here, although their densities are slightly, but systematically higher within $0.02R_{200}$. This is apparent in the second panel of Fig. 2, which shows how the median value of $\rho_{\text{exsitu}}/\rho_{\text{exsitu}}^{\text{CDM}}$ and its scatter vary across DM models as a function of distance from the centre. Overall, we find that $\rho_{\text{exsitu}}^{\text{WDM}}/\rho_{\text{exsitu}}^{\text{CDM}} = 1.4^{+0.6}_{-0.6}$ at the smallest radii we consider. The large scatter across systems makes the spatial dis-

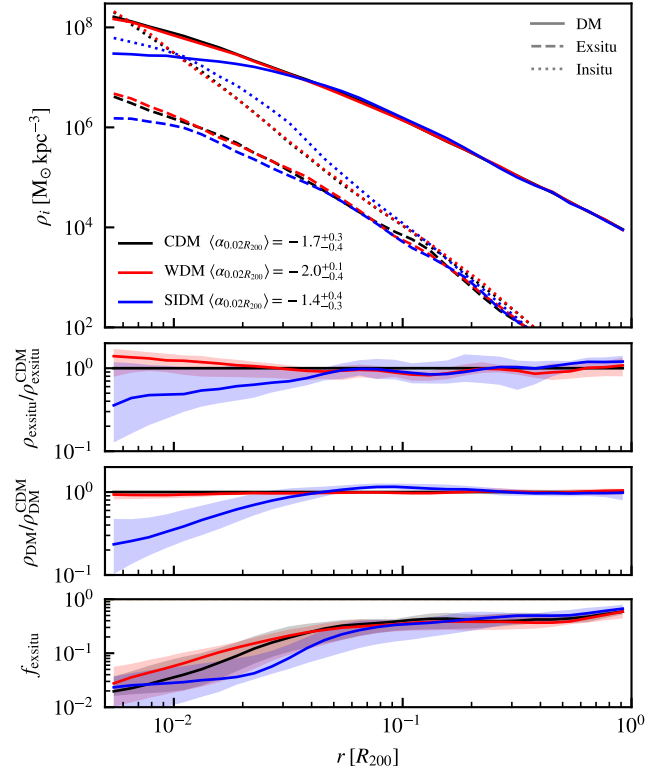


Figure 2. Top panel: median 3D density profiles of the ex-situ (dashed) and in-situ (dotted) stellar components around MW-mass haloes, as well as its DM component (solid). This is shown across their CDM (black), WDM (red) and SIDM (blue) variants. Middle panels: median ratio of the ex-situ stellar and DM density at a given spherical shell across DM variants, relative to their values in the CDM counterparts. Bottom panel: median differential ex-situ density relative to the total stellar density, as a function of distance to the centre. The distributions shown in the bottom three panels have been smoothed using a linear Savitzky–Golay filter over three consecutive bins, and the shaded regions indicate the 16th to 84th percentiles.

tribution of accreted stellar haloes in WDM consistent with CDM, when taken as an ensemble.

This study is not the first one to consider how the accreted stellar populations around MW-mass haloes change in a warm dark matter model. Previous work by Power & Robotham (2016) found differences in the distribution of stellar material between CDM and WDM, with warmer models resulting in a stronger suppression in the total stellar density beyond $r > 0.1R_{200}$. In their warmest model, $m_{\text{th}} = 0.5 \text{ keV}$, the density decreased by an order a magnitude, whereas it was comparable to CDM for their $m_{\text{th}} = 2.0 \text{ keV}$ model. Although in comparison with our simulations their galaxy sample was smaller, the mass resolution lower and the galaxy formation physics different, our findings are consistent with their coldest model. Indeed, we see no differences in the stellar density between WDM and CDM beyond $0.1R_{200}$, as shown in the top panel of Fig. 2.

Unsurprisingly, the in-situ stellar and dark matter density profiles of the WDM model are consistent with the CDM counterparts across the whole radial range we consider. We show these density profiles in the top panel of Fig. 2, which we measured using the same binning scheme as that employed for the accreted component. The similarity in the density distribution of the central galaxy and its host dark matter halo is expected. The mass scale affected by our chosen cut-off in the power spectrum is orders of magnitude lower than MW-mass scales. This means that the formation of the host DM halo is not affected by

a delay in its formation, and so its structural parameters are largely the same in CDM and WDM. As the galaxy formation model is the same, the galaxies that form at its centre are very similar.

Shifting to the SIDM model, it is apparent that the outskirts of the ex-situ density profiles are similar to those in CDM. However, contrary to what we find in WDM, the ex-situ stellar density is strongly suppressed in the central $0.05R_{200}$. The radial dependence of the accreted density is also different than the corresponding CDM and WDM counterparts, appearing significantly flatter towards the centre. To quantify how much the slope has changed, we fit a power law, $\rho \propto r^\alpha$, to the ex-situ profiles within $0.02R_{200}$. We do this for both CDM and SIDM, measuring a median value in our sample of $\langle\alpha_{\text{CDM}}\rangle = -1.7^{+0.3}_{-0.4}$ and $\langle\alpha_{\text{SIDM}}\rangle = -1.4^{+0.4}_{-0.3}$. Despite the large scatter in the slopes, the accreted stellar mass profiles are systematically flatter in SIDM than in CDM. Beyond the slope of the profiles, the central ($r \sim 0.01R_{200}$) ex-situ density decreases to a value of $\rho_{\text{exsitu}}^{\text{SIDM}}/\rho_{\text{exsitu}}^{\text{CDM}} = 0.3^{+0.9}_{-0.2}$ relative to the CDM counterparts, with some stellar haloes having an order of magnitude lower in density.

As stellar haloes are tracers of the underlying gravitational potential field, we explore how the changes in the spatial distribution of accreted stars in SIDM compare to the DM halo of their host galaxy. The median ratio of the DM density profiles in SIDM relative to CDM is plotted in the second-to-last panel of Fig. 2. Here we see that the suppression in the DM density at $0.01R_{200}$ ($\rho_{\text{DM}}^{\text{SIDM}}/\rho_{\text{DM}}^{\text{CDM}} = 0.2^{+0.2}_{-0.1}$) is stronger and less variable than that observed in the accreted stellar densities. The scale on which the expansion is present in both the DM and accreted stellar components is similar.

We also highlight the fact that the in-situ stellar component exhibits differences relative to their counterparts in CDM and WDM (see top panel of Fig. 2). In particular, their central densities are lower than the corresponding galaxies formed in CDM and WDM, with a slight enhancement in the outskirts of the galaxy ($r \sim 0.01$ to $0.1R_{200}$). As this is likely partly driven by the shallower potential well present in the host, it will be interesting to explore in the future how the perturbative effect of mergers and fly-bys differ in the formation process of in-situ stellar haloes in SIDM cosmologies.

Nonetheless, the magnitude and shape of the ex-situ and in-situ expansion differ between each other, leading to different local ex-situ mass fractions, $f_{\text{exsitu}} = \rho_{\text{exsitu}}/\rho_*$, as a function of radius. The median values measured across our sample are shown in the bottom panel of Fig. 2, where we see that the radial dependence in SIDM is substantially different to CDM and WDM. Its value is always lower in the spatial range where the halo has expanded ($r < 0.05R_{200}$), and retains a constant value within $\sim 0.02R_{200}$ instead of increasing like in CDM and WDM.

We confirm that the way in which accreted stellar material is distributed within $0.05R_{200}$ varies depending on the assumed dark matter model. For WDM (SIDM), the inner regions of the accreted stellar halo are more (less) dense than in CDM, with the most extreme examples having $\rho_{\text{exsitu}}^{\text{WDM}}/\rho_{\text{exsitu}}^{\text{CDM}} = 2.56$ and $\rho_{\text{exsitu}}^{\text{SIDM}}/\rho_{\text{exsitu}}^{\text{CDM}} = 0.05$ at $0.01R_{200}$. Together with the fact that the overall ex-situ mass remains similar across models, these changes suggest a rearrangement of the accreted material, and hence how spatially concentrated it is distributed. Since the spatial distribution of stars reflects their underlying orbit distribution, these differences motivate a closer look at their velocity distributions. Additionally, phase-space signatures originating from major accretion and stripping events might differ relative to CDM, reflecting the change in the rate with which bound mass is lost and the number of accretions that result from the alternative DM variants used in this work. We explore this in the following subsection.

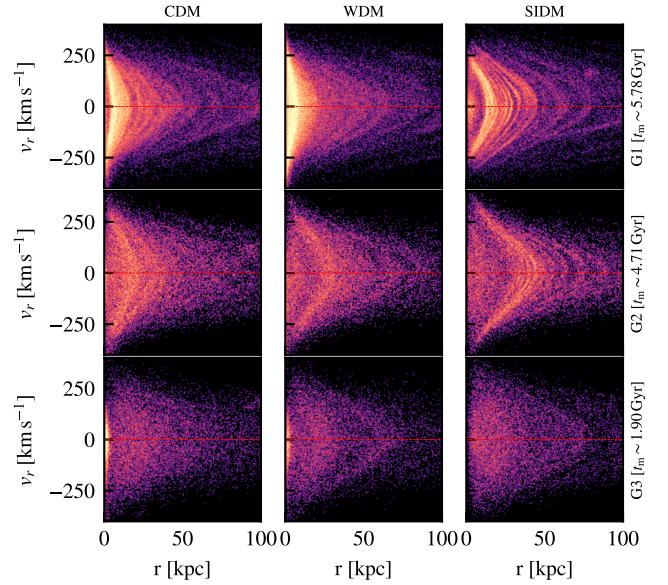


Figure 3. Radial velocity of accreted stellar particles, as a function of their radial distance to the centre of their host galaxies. The colour of each particle encodes the local ex-situ stellar density. This is shown for three $z = 0$ haloes (top to bottom) across their matched CDM, WDM and SIDM versions (left to right). The vertical ordering reflects the ease with which differences can be identified across DM models, with their IDs (G1, G2 and G3) shown on the right hand side. The approximate time at which each galaxy experienced its last major merger is also indicated on the right-hand axis, which is similar across DM models (see Table 1).

4.3 Kinematics

To investigate how the velocity distribution of the ex-situ stellar halo changes across DM models, we first compare three representative galaxies from our sample. They were chosen based on the fact that no disruptions of massive satellites have occurred in the recent past, providing a view into how a relaxed stellar halo looks like. We show in Fig. 3 how the radial velocity of ex-situ stars, v_r , vary as a function of their distance to the centre, r . From hereon, we refer to these examples as G1, G2 and G3, which is intended to represent the relative ease with which differences in the kinematics of accreted stars can be visually identified across DM models. The v_r vs r distributions for the rest of the MW-mass haloes in our sample are shown in Fig. B1.

Several ‘chevrons’ – i.e. overdensities in r, v_r space – are present in G1 and G2, whereas the distribution of G3 is largely smooth and featureless. Chevrons reflect apocentre pileups of stars that have been stripped from their progenitor galaxy, so their number and location encode information about the stripping history of the progenitor satellite that gave rise to them (e.g. Dong-Páez et al. 2022). The subsequent evolution is governed by interactions with the local environment (e.g. Davies et al. 2023a,b) and Liouville’s theorem, whereby chevrons progressively wind up in position and velocity space until they can no longer be distinguished from one another nor the background.

Focusing on the first two examples, it is clear that the number of chevrons varies according to the assumed dark matter model, with WDM having the fewest and SIDM having the most. The thickness of each individual chevron also changes with the assumed dark matter model, with the thinnest chevrons being present in SIDM. In line with the spatial distribution of the accreted stellar halo, the SIDM chevrons are typically found at larger radii than in the other two models. Since this entails longer dynamical timescales, the time for

Event	Model	Mass ratio	t_{infall} [Gyr]	t_{merge} [Gyr]	Δt [Gyr]
G1/M1	CDM	0.41	5.78	9.76	4.0
	WDM	0.46	5.78	10.04	4.3
	SIDM	0.46	5.78	8.94	3.2
G1/M2	CDM	0.28	3.12	5.95	2.8
	WDM	0.36	2.8	6.15	3.4
	SIDM	0.28	3.12	5.04	1.9
G2/M1	CDM	0.17	4.71	7.93	3.2
	WDM	0.2	4.71	8.17	3.5
	SIDM	0.21	4.71	7.68	3.0
G3/M1	CDM	0.06	1.9	3.84	1.9
	WDM	0.07	1.32	3.97	2.7
	SIDM	0.08	1.9	2.19	0.3

Table 1. Summary properties of the last major mergers experienced by the three examples shown in Fig. 3, identified independently across the DM variants considered in this work. The infall time, t_{infall} , corresponds to when the merged object first became a satellite of the main progenitor. We measure the merger mass ratio in the output immediately prior to this time, before significant tidal stripping occurs. The merger is complete at t_{merge} , which we identify as the time when the object no longer had a resolved bound component. The time elapsed between infall and accretion is shown in the rightmost column.

the chevrons to fold and mix with the background is expected to be longer in SIDM than in WDM and CDM.

To put these examples in perspective with respect to the rest of the sample of stellar haloes used in this study, we highlight with green circles their ex-situ masses in Fig. 1. Their masses bracket that of the overall sample, and the ordering based on the visual comparison of the differences in the number and prominence of chevrons reflects their mass ranking. Since the mass of stellar haloes typically correlate to their formation time, we proceed to identify when the stellar haloes of G1, G2 and G3 formed.

Our operational definition for the formation time of the accreted stellar halo is based on when the last major merger occurred. To identify when this happened, we follow the merger tree of every MW-mass halo in our sample, and identify all objects that directly merged onto its main progenitor branch. We then compute the mass ratio between the merged object and the main progenitor, f_{merge} , at the time before the stellar halo progenitor became a satellite of the host for the first time. This avoids underestimating the merger mass ratio due to subsequent mass loss and growth of the host. In practice, we use the FoF group membership to identify when the stellar halo progenitor and the host main progenitor are in the same FoF group, which we use as our definition of accretion. Finally, we select all luminous objects with $f_{\text{merge}} \geq 0.1$, and inspect their evolution to check whether it was indeed a major merger. If no candidates are found, we progressively lower the threshold until one is identified. This was only needed for example G3, which formed early and hence had a less trivial analysis.

The resulting formation times of the stellar haloes of G1, G2 and G3 are $t_{\text{form}} \equiv t_{\text{infall}} \sim 5.78, 4.71, 1.90$ Gyr, respectively. There is little to no variation in when these occur across DM models, aside from G3, which we attribute to the aforementioned difficulty associated to its early forming nature. By identifying the formation time, we see that the magnitude of the differences in the abundance and prominence of chevrons across DM models reflects the age of

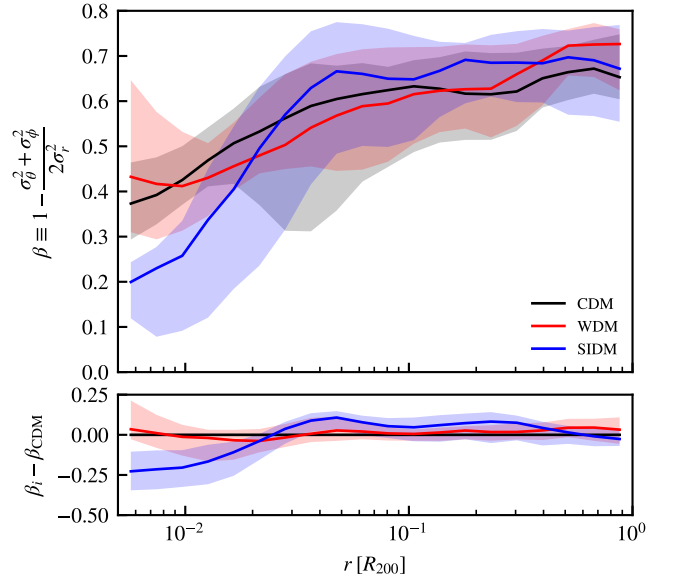


Figure 4. *Top panel:* velocity anisotropy of the ex-situ stellar component around the MW-mass haloes in our sample, across CDM (black), WDM (red) and SIDM (blue) models. The shaded regions indicate the 16th - 84th percentiles and the solid lines the median values. Both have been smoothed using a linear Savitzky–Golay filter over three consecutive bins. *Bottom panel:* same as above, but showing the median difference in the velocity anisotropy across matched counterparts, and the associated 16th - 84th percentiles.

the accreted stellar halo, with the largest changes present in later forming stellar haloes. Even if differences existed shortly after the last major merger occurred, the subsequent evolution of chevrons makes any initially existing ones mix beyond our visual identification capabilities.

This still raises the question of how the differences arise across models. To answer this, we follow the evolution of the primary progenitors of the stellar halo of G1, G2 and G3 after they are accreted. The masses and times when they are accreted are similar across models, as seen in Table 1. However, there are structural differences in the SIDM haloes resulting from self-interactions. The differences are present as flat density cores in the DM haloes hosting the progenitor galaxies of the stellar halo, as well as the velocity distribution of the stellar particles bound to them. In WDM, the main progenitors of these three stellar haloes appear to be accreted with slightly different radial velocities and timings than those in CDM and SIDM. In other words, they are at different locations in r, v_r space than the corresponding ones in CDM and SIDM, which are more similarly located.

These differences propagate into the merging time of the progenitors, which we define to be the difference in time between their accretion and disruption³. As shown in Table 1, they vary across models in a systematic manner: SIDM subhaloes disrupt the fastest, and the WDM ones take the longest to do so. The change in SIDM is likely due to the presence of flat density cores and subhalo evaporation, which exacerbates mass loss and accelerates their disruption. In WDM, their apocentres are larger than in CDM after the first pericentric passage. This could be due to their aforementioned (small) differences in their location in r, v_r space relative to CDM, which are amplified after undergoing pericentre. Consequently, they remain

³ Defined to occur when SUBFIND is unable to identify them as self-bound structure during five consecutive outputs.

further out and their disruption takes longer. Whether this is a systematic difference always present in accreted WDM progenitors of stellar haloes, or a difference only present in the three examples discussed here, is relegated to future work.

The primary progenitors of the stellar haloes of G1, G2 and G3 have high mass ratios relative to the main progenitor of the MW-mass hosts (see Table 1). Their post-accretion evolution is therefore driven by the interplay between dynamical friction and loss of bound mass. As their masses at accretion time do not differ substantially across DM models, changing how long mergers last for could affect the integrated effect they experience from dynamical friction. Hence, the systematically different merging timescales suggest that WDM and SIDM progenitors might have experienced more or less *net* dynamical friction than the corresponding CDM counterparts. This could explain why the spatial distributions end up being slightly denser in WDM and substantially less dense in SIDM, respectively. However, as noted before, the ex-situ density changes occur on the same scale as the DM ones in SIDM. This highlights the fact that the end result could be a combination of changing dynamical friction, subhalo stripping & evaporation, and the gravitational potential of the host. Identifying which of these factors dominates is not trivial to do in the cosmological simulations we use in this work.

Galaxies that experience major mergers, as is the case during the formation of the stellar haloes of G1, G2 and G3, typically undergo orbit radialisation (e.g. Amorisco 2017; Vasiliev et al. 2022). This process removes angular momentum from the orbits of merging galaxies, making them more radial than when they were first accreted. Given the differences in how long it took for the progenitors in G1, G2 and G3 to merge across DM models, the anisotropy of accreted stars could, in principle, also change. To investigate whether this is the case, we measure the velocity anisotropy of all ex-situ stars, defined as:

$$\beta = 1 - \frac{\sigma_{\theta}^2 + \sigma_{\phi}^2}{2\sigma_r^2}, \quad (5)$$

across all haloes in our sample. We use a coordinate system where the angular momentum of all stellar particles within 5 kpc of the centre points along the z-axis. We use a similar binning scheme as the density profiles, i.e., 20 spherical shells logarithmically spaced between $0.005R_{200}$ and R_{200} , and then take the median values across our whole sample.

We show the resulting velocity anisotropy profiles in Fig 4, where the WDM profile is very similar to the one measured in the CDM version. In contrast, the SIDM profile exhibits clear differences with respect to CDM and WDM. We believe the differences are driven by shorter merging timescales and shallower density profiles, with the former being particularly important as it decreases the time during which orbit radialisation can occur. On the other hand, their CDM and WDM counterparts take longer to merge, giving radialisation more time to make the progenitor orbits more eccentric, and hence result in more radially supported accreted stellar haloes.

The fact that such a difference exists is striking, and highlights the potential usefulness of the Gaia-Sausage-Enceladus (GE/S) debris as a DM constraint. In other words, given current constraints on its orbital anisotropy (e.g. $\beta \sim 0.8$; Belokurov et al. 2018), one can identify how large of an SIDM cross-section can be accommodated before radialisation becomes ineffective and no GE/S-like remnants are produced. This would provide hints on what the SIDM cross-section on scales between MW-mass and dwarf-mass scales is, corresponding to the transition region for velocity-dependent cross-sections.

In summary, we have seen that both the spatial and velocity distribution of the ex-situ stellar component depends on the assumed

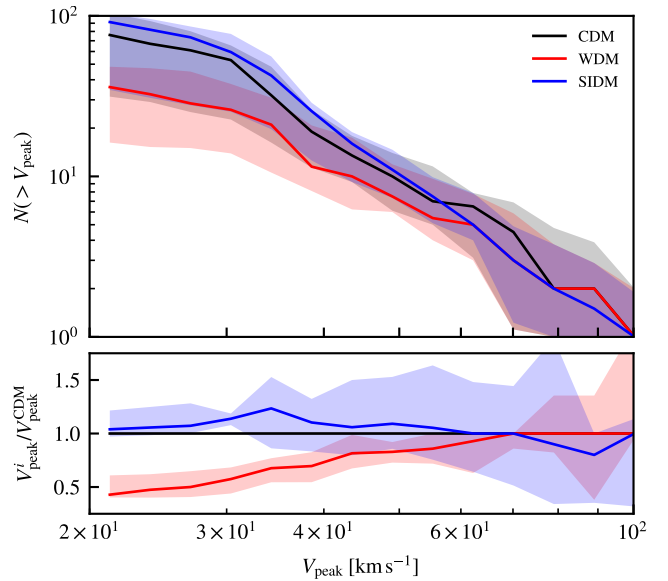


Figure 5. *Top panel:* distribution of the peak maximum circular velocity of the galaxies that directly merge with the MW-mass main progenitors, which we take as the building blocks of their stellar halo. This is shown across different DM models, as indicated by the top right legend. The solid lines indicate the median values across our population, with the shaded regions showing the 16th and 84th percentiles of the distribution. *Bottom panel:* same as above, but for the median difference across matched counterparts. See Fig. A1 for the corresponding peak stellar mass distributions.

model of dark matter. To understand the reason why different models result in changing properties, it is crucial to investigate how the properties of its building blocks vary across models, both prior to being accreted (e.g. peak mass), and during stripping and merging (e.g. stellar deposition radii). We do so in the following subsection.

4.4 The building blocks

The dynamical and spatial differences of present-day stellar haloes reflect the properties of accreted objects and the host assembly history. Given that we have considered the same sample of Milky Way-mass haloes, whose counterparts share the same overall assembly histories, the relative differences in the spatial and velocity distributions of stellar haloes are due to changes in the population of accreted haloes and the manner in which they contribute stars towards their build-up. We already showed this explicitly for examples G1, G2 and G3, but we now extend our analysis to see how the mass spectrum of stellar halo progenitors, as well as orbital energies, change across our whole sample of MW-mass haloes.

To find which galaxies contributed to the build up of the stellar haloes in our sample, we identify all luminous structures whose main merger tree branches directly merge with the main progenitor of each MW-mass halo. We show in Fig. 5 the resulting V_{peak}^4 function of the population we find, which is a proxy for halo mass, and hence stellar mass.

Focusing on the total number of disrupted objects, we note there are significant changes across dark matter models. The lowest number corresponds to the WDM model, where the suppression reflects lower numbers of galaxies forming, and hence less discrete contributions to

⁴ Defined as the peak value of the maximum circular velocity of a subhalo, $V_{\text{circ}} = \sqrt{GM(< r)/r}$, as measured across its main progenitor branch.

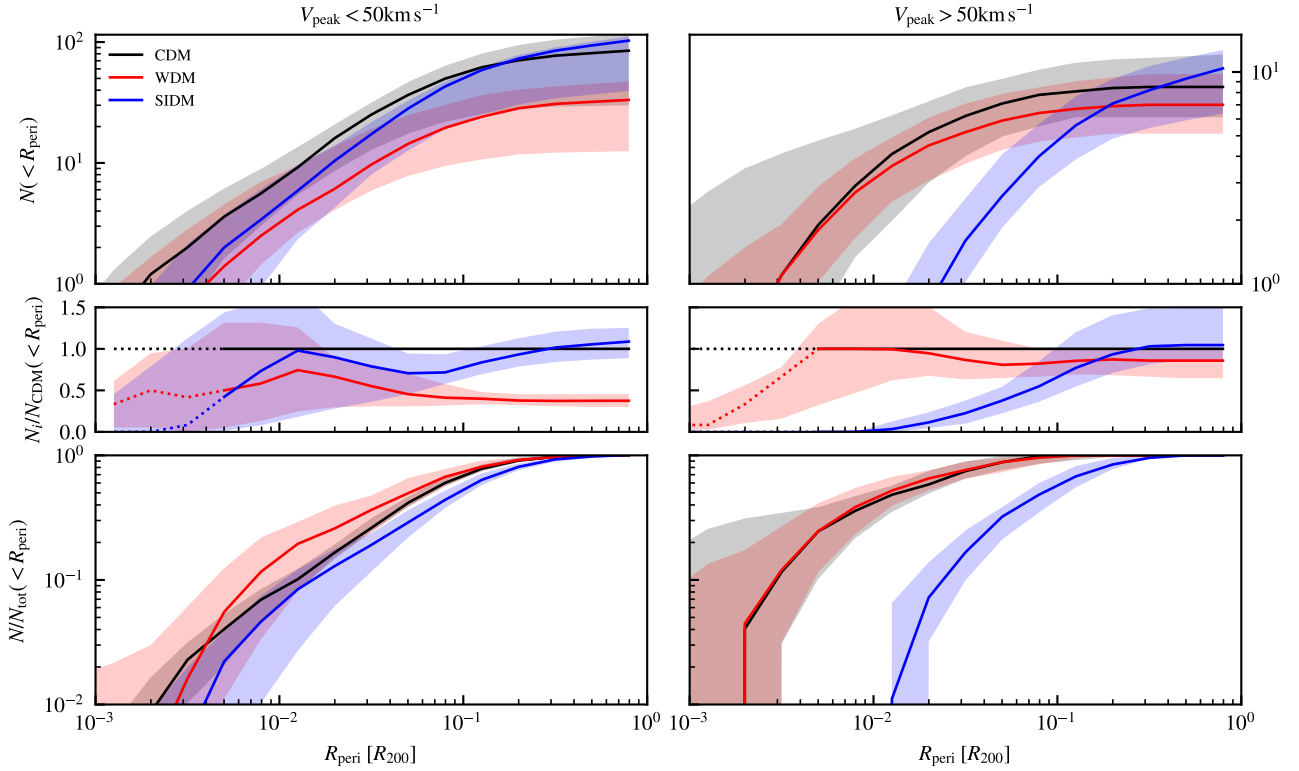


Figure 6. Cumulative distribution function of the pericentric distances of the stellar halo progenitors before they disrupted. They are classified into two V_{peak} bins, according to whether they have values larger (right column) or lower (left column) than 50 km s^{-1} . *Top panel:* median distribution, with shaded regions bracketing the 16th and 84th percentiles. *Middle panel:* same as above, but expressed relative to the value of their matched CDM counterpart. The dashed line indicates the scale at which at least one CDM counterpart reaches a value of zero, and hence where the median ratios start becoming dominated by fewer objects. *Bottom panel:* same as the two panels above, but normalised to the total number of objects within R_{200} . All these distributions have been smoothed using a linear Savitzky–Golay filter over three consecutive bins.

the build-up of the stellar halo. The largest number of progenitors are present in SIDM, since it forms the same amount of structure as in CDM (their power spectra are assumed to be the same in this study), but the structural changes and scatterings with the background DM of the host result in more efficient mass loss, and hence larger numbers of disrupted subhaloes.

The differences discussed in §4.2 and §4.3 concern the inner region of the stellar halo, and so are likely to be driven by its most massive progenitors. However, no significant differences are present in this mass range across models, which are all consistent within their 16th - 84th percentiles. As the models we have used here primarily affect their internal structure, or the masses and abundances of less massive haloes, the total masses of the largest contributors are unaffected, and how much mass they deposit remains similar.

However, the evolution of these massive objects prior to disruption can still vary. For example, a galaxy that experiences more tidal stripping whilst sinking towards the centre of its host, will result in stars with higher energy orbits and generally less circular orbits compared to one that is not as easily stripped. This will subsequently alter the orbital distributions of the stars, and hence their spatial and dynamical distribution. As such, we investigate this by examining the typical pericentric distance of progenitor galaxies just before they disrupted. Although galaxies deposit stars on a range of orbital energies, this metric provides an estimate on the lowest orbital energies on which stripped stars get placed onto.

To do this, we integrate the orbits in the particle potential around the MW-mass main progenitor. The potential is fit to the particle

distribution using AGAMA (Vasiliev 2019) and assuming a spherically symmetric potential for the stars, gas and dark matter particles. We believe that this assumption, though approximate, is sufficient to capture the major trends in the population we study here. As initial conditions, we use the relative position and velocity between the stellar halo progenitors and the MW-mass main progenitor, measured at the output when the former were last identified as self-bound by SUBFIND.

The resulting distribution of pericentric distances estimated at the time before disruption is shown in Fig. 6. Since the mass of the progenitor is an important indicator for whether they dominate the mass budget of the stellar halo, we split the distribution into two based on whether their V_{peak} is greater or lower than 50 km s^{-1} . We also show these distributions normalised to the total number of stellar halo progenitors, to decouple the suppression of structure in WDM from the distribution of their disruption distances.

As the overall properties of the stellar halo are set by those with the highest V_{peak} values, we focus first on the $V_{\text{peak}} > 50 \text{ km s}^{-1}$ bin. Despite a similar number of progenitors across DM models, the shape of the distributions are very different. The clearest change occurs in SIDM, where most objects disrupt at larger pericentric distances than CDM and WDM. Since the initial orbital properties are expected to be similar to CDM, the differences arise due to the subsequent orbital evolution and mass loss that the satellite galaxies experienced. As argued previously, the faster mass loss rates lead to an earlier disruption, and hence potentially lessened effects of dynamical friction and radialisation. This would generally result in

their stellar remnants retaining higher orbital energy and being less radially supported than in CDM, as discussed in §4.2 and §4.3.

There are essentially no changes in the WDM case, with the main one being one less galaxy typically contributing to the high V_{peak} distribution. Nonetheless, after normalising by the total number of progenitors we find that the distribution is the same as in CDM in the inner parts. The minor differences between the ex-situ density profiles in CDM and WDM, as well as the velocity anisotropy of the stellar halo, reflect the similarity in the distributions we find here.

Differences in the lower V_{peak} distribution occur primarily in the number of building blocks. As expected, the WDM counterpart is heavily suppressed relative to CDM and SIDM, and its overall distribution is more centrally concentrated. Although subhaloes disrupt at larger distances in SIDM, the difference relative to CDM is not as large as in the $V_{\text{peak}} > 50 \text{ km s}^{-1}$ bin. Nonetheless, this does not preclude the presence of different stellar stream properties caused by different mass loss efficiencies, which we have not explored in the present work.

5 CONCLUSIONS

We have used the cosmological hydrodynamical simulations presented in Forouhar Moreno et al. (2022), which follow the assembly of Milky Way-mass haloes across a variety of dark matter models, to explore the effect that different DM models have on the properties of accreted stellar haloes. For this purpose, we identified the accreted stellar population around eight haloes with present-day virial masses between $5 \times 10^{11} M_{\odot}$ and $2.5 \times 10^{12} M_{\odot}$. Using all accreted stars as our definition of the stellar halo, our findings are as follows:

- The overall accreted stellar mass remains similar across the DM models we considered in this study (Fig. 1). Since this mass is largely established by its most massive progenitors, and in particular their stellar mass, this suggests that neither DM self-interactions nor the suppression in the DM power spectrum we consider here affect their overall mass properties. This is true so long as the resulting power spectrum cut-off does not affect the formation of the main stellar halo progenitors.

- The spatial distribution of stellar haloes is more sensitive to the assumed model of dark matter, and are largely present in the inner parts (Fig. 2). This is most evident for the SIDM model, where the differences already appear within $0.05R_{200}$ ($\sim 10 \text{ kpc}$), coinciding with the spatial scale where the DM density profile has flattened due to self-interactions. The changes manifest as a reduction of the accreted stellar density to a median value of $\langle \rho_{\text{exsitu}}^{\text{SIDM}} / \rho_{\text{exsitu}}^{\text{CDM}} \rangle = 0.3^{+0.9}_{-0.2}$ of its CDM counterparts, as well as shallower density profiles: $\langle \alpha_{\text{SIDM}} \rangle = -1.4^{+0.4}_{-0.3}$ vs $\langle \alpha_{\text{CDM}} \rangle = -1.7^{+0.3}_{-0.4}$. In WDM, the profiles change in the opposite direction than SIDM, being instead slightly denser, $\langle \rho_{\text{exsitu}}^{\text{WDM}} / \rho_{\text{exsitu}}^{\text{CDM}} \rangle = 1.4^{+0.6}_{-0.6}$, and steeper, $\langle \alpha_{\text{WDM}} \rangle = -2.0^{+0.1}_{-0.4}$ than the CDM counterparts. However, the changes in the WDM ex-situ density are minor compared to those observed in the SIDM model.

- Beyond their density profiles, the velocity distribution of accreted stars also differs across models. This results in a larger number and prominence of overdensities in r, v_r space (Fig. 3) and more tangentially supported orbits in SIDM than in CDM (Fig. 4). This amounts to a typical change in the velocity anisotropy of $\langle \Delta\beta \rangle = -0.2^{+0.1}_{-0.1}$ between SIDM and CDM in the inner $0.01R_{200}$ ($\sim 2 \text{ kpc}$). The changing anisotropy could be used in conjunction with the properties of the GE/S in the Milky Way to place upper limits on the allowed SIDM cross-section. In other words, what is

the maximum possible value of σ_{SIDM} that can accommodate highly radially supported ($\beta \sim 0.8$) remnant of GE/S-like events. This will be explored in upcoming work.

To understand the origin behind these differences, we identified the progenitors of the stellar haloes we studied here. In this work, we defined them to be any disrupted galaxy whose descendant was the main progenitor of the haloes hosting the stellar haloes we studied.

- We first discussed three representative examples that bracket the mass range of our selected sample, illustrating how the assumed dark matter model affects their merging timescales. As shown in Table 1, these vary in a systematic manner, with SIDM and WDM taking the shortest and longest times to merge, respectively.

- The lowest number of progenitors is present in WDM, reflecting the suppression in the amount of galaxies that form and hence accretions onto the simulated MWs. On the other hand, SIDM haloes suffer from enhanced mass loss, and so a larger number of them contribute toward the build up of stellar halo. However, these changes are relegated to the lowest mass progenitors, and hence do not contribute to the differences we discuss in this work.

- Given the changes in merging timescales, and hence the time that dynamical friction and radialisation have to operate, we examined how the final orbital energy of progenitors changed across models. For this purpose, we measured their pericentre values before disruption as a proxy for their final orbital energy. In doing so, we found that progenitors in SIDM have significantly larger pericentric values at disruption than CDM or WDM. Together with the expansion of the host DM halo, this constitutes another difference that can lead to the observed decrease in the central ex-situ density.

Several assumptions and limitations are present in this study. Firstly, we have considered simulations in which the predicted differences between dark matter models are exacerbated, i.e. no flat-density core formation through gas blowouts in dwarf galaxies. As shown in Forouhar Moreno et al. (2022), this process can mimic the effects of SIDM on the satellite population, and could therefore similarly affect the most massive stellar halo progenitors and thus its final properties. It nonetheless remains to be seen whether baryon-driven outflows are effective at forming flat density cores for massive GE/S-like galaxies at high redshifts. Secondly, we have used relatively extreme variations in the nature of dark matter, and so follow-up work should consider versions that are more consistent with current observational constraints. Lastly, our comparisons between dark matter models do not include observational uncertainties. This means that the differences we identified in this work may be difficult to observe in the real Universe. As such, mock observations should be made based on these simulations, to enable a fairer comparison to real data.

Despite these caveats, our findings highlight a new potential avenue to constrain the nature of dark matter, based on the dynamics and distribution of the accreted stellar halo of Milky Way-mass galaxies. One approach would be to measure the spatial distribution of the stellar halo around a large sample of MW-like galaxies in the Universe, and compare it to the predicted distribution across different DM models. An alternative would be to leverage the phase-space information of GE/S, by identifying simulated MW-analogues that experienced similar events in their past and measuring the final velocity anisotropy of its remnant. As changing the value of the SIDM cross-section systematically affects the merging process, and hence the anisotropy β , comparing the predicted distributions of β to the one observed for GE/S could hint at which SIDM cross-sections are compatible with the data.

Beyond these two approaches, one can imagine other observables

which we have not considered and could be similarly affected, such as the two-point correlation function in phase-space, clustering in action space, and metallicity gradients. Given ongoing and upcoming efforts towards studying the stellar halo Milky Way and those of external Milky Way-mass haloes, this exciting prospect warrants further investigation.

ACKNOWLEDGEMENTS

VJFM acknowledges support by NWO through the Dark Universe Science Collaboration (OCENW.XL21.XL21.025) and the European Research Council (ERC) through the Advanced Investigator grant DMIDAS (GA 786910) and Consolidated Grant ST/T000244/1. A.B.L. acknowledges support from the European Research Council (ERC) under the European Union's Horizon 2020 research and innovation program (GA 101026328). AD is supported by a Royal Society University Research Fellowship and the Leverhulme Trust. AD and AF acknowledge support from the Science and Technology Facilities Council (STFC) [grant numbers ST/X001075/1, ST/T000244/1]. AF is supported by a UKRI Future Leaders Fellowship (grant no MR/T042362/1). This work used the DiRAC@Durham facility managed by the Institute for Computational Cosmology on behalf of the STFC DiRAC HPC Facility (www.dirac.ac.uk). The equipment was funded by BEIS capital funding via STFC capital grants ST/K00042X/1, ST/P002293/1, ST/R002371/1 and ST/S002502/1, Durham University and STFC operations grant ST/R000832/1. DiRAC is part of the National e-Infrastructure.

DATA AVAILABILITY

The data used in this study can be made available upon reasonable request to the corresponding author.

REFERENCES

- Abadi M. G., Navarro J. F., Steinmetz M., 2006, *MNRAS*, **365**, 747
 Amorisco N. C., 2017, *MNRAS*, **464**, 2882
 Aprile E., et al., 2018, *Phys. Rev. Lett.*, **121**, 111302
 Bell E. F., et al., 2008, *ApJ*, **680**, 295
 Belokurov V., Erkal D., Evans N. W., Koposov S. E., Deason A. J., 2018, *MNRAS*, **478**, 611
 Benítez-Llambay A., Frenk C., 2020, *MNRAS*, **498**, 4887
 Bode P., Ostriker J. P., Turok N., 2001, *ApJ*, **556**, 93
 Booth C. M., Schaye J., 2009, *MNRAS*, **398**, 53
 Bose S., et al., 2017, *MNRAS*, **464**, 4520
 Bovy J., Bahmanyar A., Fritz T. K., Kallivayalil N., 2016, *ApJ*, **833**, 31
 Boyarsky A., Ruchayskiy O., Iakubovskiy D., Franse J., 2014, *Phys. Rev. Lett.*, **113**, 251301
 Brook C. B., Di Cintio A., Knebe A., Gottlöber S., Hoffman Y., Yepes G., Garrison-Kimmel S., 2014, *ApJ*, **784**, L14
 Bullock J. S., Johnston K. V., 2005, *ApJ*, **635**, 931
 Buschmann M., Kopp J., Safdi B. R., Wu C.-L., 2018, *Phys. Rev. Lett.*, **120**, 211101
 Callingham T. M., et al., 2019, *MNRAS*, **484**, 5453
 Canepa A., 2019, *Reviews in Physics*, **4**, 100033
 Cautun M., et al., 2020, *MNRAS*, **494**, 4291
 Chandrasekhar S., 1943, *ApJ*, **97**, 255
 Cole S., et al., 2005, *MNRAS*, **362**, 505
 Conroy C., et al., 2019, *ApJ*, **883**, 107
 Cooper A. P., Parry O. H., Lowing B., Cole S., Frenk C., 2015, *MNRAS*, **454**, 3185
 Cooper A. P., et al., 2023, *ApJ*, **947**, 37
 Crain R. A., et al., 2015, *MNRAS*, **450**, 1937
 Cyr-Racine F.-Y., Sigurdson K., Zavala J., Bringmann T., Vogelsberger M., Pfrommer C., 2016, *Phys. Rev. D*, **93**, 123527
 Dalla Vecchia C., Schaye J., 2012, *MNRAS*, **426**, 140
 Davé R., Spergel D. N., Steinhardt P. J., Wandelt B. D., 2001, *ApJ*, **547**, 574
 Davies E. Y., Vasiliev E., Belokurov V., Evans N. W., Dillamore A. M., 2023a, *MNRAS*, **519**, 530
 Davies E. Y., Dillamore A. M., Vasiliev E., Belokurov V., 2023b, *MNRAS*, **521**, L24
 Davis M., Efstathiou G., Frenk C. S., White S. D. M., 1985, *ApJ*, **292**, 371
 De Lucia G., Blaizot J., 2007, *MNRAS*, **375**, 2
 Deason A. J., Belokurov V., Evans N. W., Johnston K. V., 2013, *ApJ*, **763**, 113
 Deason A. J., Belokurov V., Sanders J. L., 2019, *MNRAS*, **490**, 3426
 Deason A. J., et al., 2021, *MNRAS*, **501**, 5964
 Deason A. J., Bose S., Fattahi A., Amorisco N. C., Hellwing W., Frenk C. S., 2022, *MNRAS*, **511**, 4044
 Di Cintio A., Brook C. B., Dutton A. A., Macciò A. V., Stinson G. S., Knebe A., 2014, *MNRAS*, **441**, 2986
 Diemand J., Madau P., Moore B., 2005, *MNRAS*, **364**, 367
 Dong-Páez C. A., Vasiliev E., Evans N. W., 2022, *MNRAS*, **510**, 230
 Eggen O. J., Lynden-Bell D., Sandage A. R., 1962, *ApJ*, **136**, 748
 Ellis J., Hagelin J. S., Nanopoulos D. V., Olive K., Srednicki M., 1984, *Nuclear Physics B*, **238**, 453
 Erkal D., et al., 2021, *MNRAS*, **506**, 2677
 Errani R., Navarro J. F., Peñarrubia J., Famaey B., Ibata R., 2022, *Monthly Notices of the Royal Astronomical Society*, **519**, 384
 Evans T. A., Fattahi A., Deason A. J., Frenk C. S., 2020, *MNRAS*, **497**, 4311
 Fattahi A., et al., 2020, *MNRAS*, **497**, 4459
 Font A. S., McCarthy I. G., Crain R. A., Theuns T., Schaye J., Wiersma R. P. C., Dalla Vecchia C., 2011, *MNRAS*, **416**, 2802
 Forouhar Moreno V. J., Benítez-Llambay A., Cole S., Frenk C., 2022, *MNRAS*, **517**, 5627
 Gaia Collaboration et al., 2016a, *A&A*, **595**, A1
 Gaia Collaboration et al., 2016b, *A&A*, **595**, A2
 Gaia Collaboration et al., 2018, *A&A*, **616**, A1
 Gaia Collaboration et al., 2023, *A&A*, **674**, A1
 Genina A., Frenk C. S., Benítez-Llambay A., Cole S., Navarro J. F., Oman K. A., Fattahi A., 2019, *MNRAS*, **488**, 2312
 Genina A., Deason A. J., Frenk C. S., 2023, *MNRAS*, **520**, 3767
 Gilbert K. M., et al., 2014, *ApJ*, **796**, 76
 Graus A. S., Bullock J. S., Kelley T., Boylan-Kolchin M., Garrison-Kimmel S., Qi Y., 2019, *MNRAS*, **488**, 4585
 Guzmán et al. R., 2022, ARRAKIHs Proposal
 Hahn O., Abel T., 2011, *MNRAS*, **415**, 2101
 Helmi A., White S. D. M., 1999, *MNRAS*, **307**, 495
 Helmi A., Babusiaux C., Koppelman H. H., Massari D., Veljanoski J., Brown A. G. A., 2018, *Nature*, **563**, 85
 Ibata R. A., Lewis G. F., Irwin M. J., Quinn T., 2002, *MNRAS*, **332**, 915
 Ivezić Ž., et al., 2019, *ApJ*, **873**, 111
 Jethwa P., Erkal D., Belokurov V., 2018, *MNRAS*, **473**, 2060
 Jiang L., Helly J. C., Cole S., Frenk C. S., 2014, *MNRAS*, **440**, 2115
 Jin S., et al., 2023, *MNRAS*,
 Johnston K. V., Zhao H., Spergel D. N., Hernquist L., 1999, *ApJ*, **512**, L109
 Kazantzidis S., Lokas E. L., Callegari S., Mayer L., Moustakas L. A., 2011, *ApJ*, **726**, 98
 Kennedy R., Frenk C., Cole S., Benson A., 2014, *MNRAS*, **442**, 2487
 Koppelman H. H., Helmi A., Massari D., Price-Whelan A. M., Starkenburg T. K., 2019, *A&A*, **631**, L9
 Kummer J., Kahlhoefer F., Schmidt-Hoberg K., 2018, *MNRAS*, **474**, 388
 Lovell M. R., Frenk C. S., Eke V. R., Jenkins A., Gao L., Theuns T., 2014, *MNRAS*, **439**, 300
 Ludlow A. D., et al., 2017, *Phys. Rev. Lett.*, **118**, 161103
 Majewski S. R., et al., 2017, *AJ*, **154**, 94
 Merritt A., van Dokkum P., Abraham R., Zhang J., 2016, *ApJ*, **830**, 62
 Monachesi A., et al., 2019, *MNRAS*, **485**, 2589
 Nadler E. O., et al., 2021, *Phys. Rev. Lett.*, **126**, 091101

- Naidu R. P., Conroy C., Bonaca A., Johnson B. D., Ting Y.-S., Caldwell N., Zaritsky D., Cargile P. A., 2020, *ApJ*, 901, 48
- Navarro J. F., Eke V. R., Frenk C. S., 1996, *MNRAS*, 283, L72
- Navarro J. F., Frenk C. S., White S. D. M., 1997, *ApJ*, 490, 493
- Newton O., et al., 2021, *J. Cosmology Astropart. Phys.*, 2021, 062
- Peñarrubia J., Benson A. J., Walker M. G., Gilmore G., McConnachie A. W., Mayer L., 2010, *MNRAS*, 406, 1290
- Planck Collaboration et al., 2014, *A&A*, 571, A1
- Pontzen A., Governato F., 2012, *MNRAS*, 421, 3464
- Power C., Robotham A. S. G., 2016, *ApJ*, 825, 31
- Purcell C. W., Bullock J. S., Kazantzidis S., 2010, *MNRAS*, 404, 1711
- Radburn-Smith D. J., et al., 2011, *ApJS*, 195, 18
- Read J. I., Iorio G., Agertz O., Fraternali F., 2017, *MNRAS*, 467, 2019
- Read J. I., Walker M. G., Steger P., 2018, *MNRAS*, 481, 860
- Robertson A., Massey R., Eke V., 2017, *MNRAS*, 465, 569
- Rodríguez-Torres S. A., et al., 2016, *MNRAS*, 460, 1173
- Sanderson R. E., et al., 2018, *ApJ*, 869, 12
- Schaller M., et al., 2015, *MNRAS*, 451, 1247
- Schaye J., 2004, *ApJ*, 609, 667
- Schaye J., Dalla Vecchia C., 2008, *MNRAS*, 383, 1210
- Schaye J., et al., 2015, *MNRAS*, 446, 521
- Searle L., Zinn R., 1978, *ApJ*, 225, 357
- Sestito F., et al., 2023, *arXiv e-prints*, p. arXiv:2301.13214
- Spergel D. N., Steinhardt P. J., 2000, *Phys. Rev. Lett.*, 84, 3760
- Springel V., 2005, *MNRAS*, 364, 1105
- Springel V., White S. D. M., Tormen G., Kauffmann G., 2001, *MNRAS*, 328, 726
- Springel V., Di Matteo T., Hernquist L., 2005, *MNRAS*, 361, 776
- Springel V., Frenk C. S., White S. D. M., 2006, *Nature*, 440, 1137
- Vasiliev E., 2019, *MNRAS*, 482, 1525
- Vasiliev E., Belokurov V., Evans N. W., 2022, *ApJ*, 926, 203
- Vogelsberger M., Zavala J., Cyr-Racine F.-Y., Pfrommer C., Bringmann T., Sigurdson K., 2016, *Mon. Not. Roy. Astron. Soc.*, 460, 1399
- Waller F., et al., 2023, *MNRAS*, 519, 1349
- Wang J., White S. D. M., 2007, *MNRAS*, 380, 93
- Wang J., Bose S., Frenk C. S., Gao L., Jenkins A., Springel V., White S. D. M., 2020, *Nature*, 585, 39
- Wiersma R. P. C., Schaye J., Smith B. D., 2009, *MNRAS*, 393, 99

APPENDIX A: PEAK STELLAR MASS FUNCTIONS

We compare the stellar masses of the main progenitors of the stellar haloes across models in Fig. A1, where the median peak stellar mass function is shown alongside the 1σ scatter. The peak stellar mass, M_*^{peak} , is defined as the maximum bound stellar mass that the galaxy attained before being disrupted.

APPENDIX B: RADIAL VELOCITY VS RADIAL DISTANCE OF ACCRETED STARS

We showed in Fig. 3 how the radial velocities of accreted stars in three example stellar haloes vary with distance from their centre. This subset of the eight haloes we have in our sample was chosen for illustrative purposes in §4.3. For completeness, we also show the distributions of the haloes not discussed in the main text in Fig. B1.

This paper has been typeset from a $\text{\TeX}/\text{\LaTeX}$ file prepared by the author.

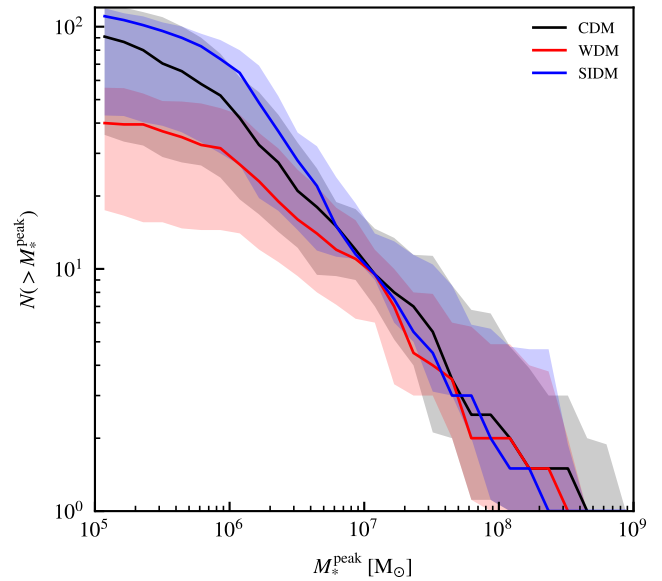


Figure A1. Similar to Fig 5, but showing instead the median peak stellar mass function of the progenitors of the stellar haloes studied in this work.

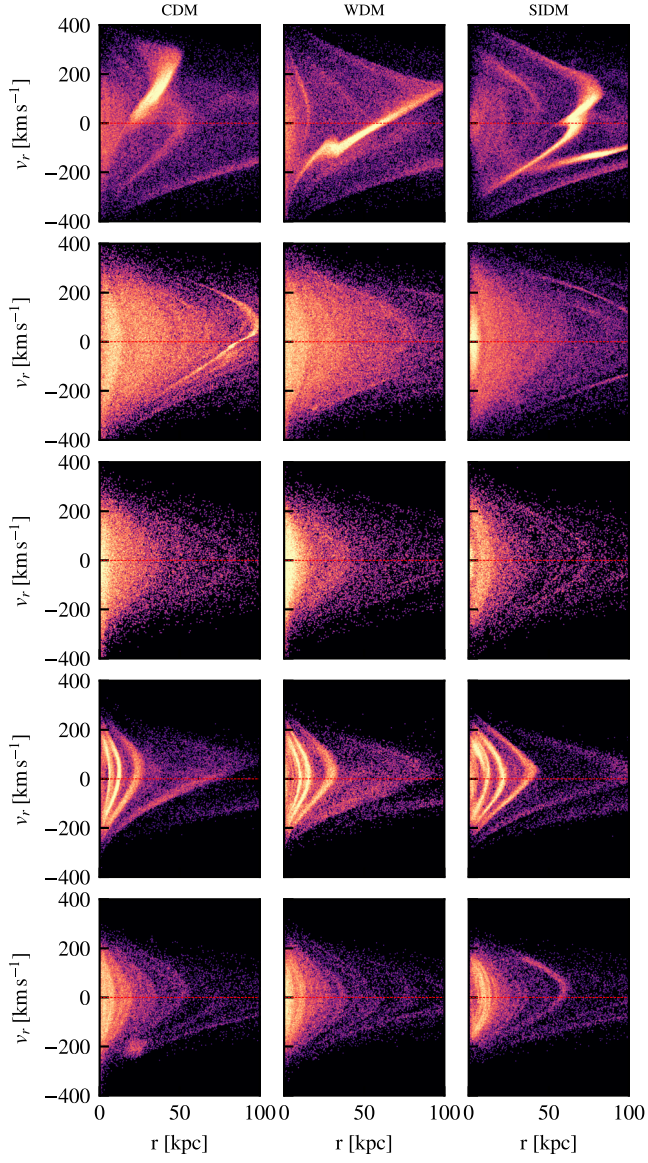


Figure B1. Radial velocity of accreted stellar particles, as a function of their radial distance to the centre of their host galaxies. The colour of each particle encodes the local ex-situ stellar density. This is shown for the remainder of the haloes not shown in Fig. 3, with their their matched CDM, WDM and SIDM versions placed from left to right. The vertical ordering reflects the $M_{200}(z=0)$ ranking, with decreasing mass towards the lower panels.